

Pieces of evidence for multiple progenitors of Swift long gamma-ray bursts

Yan-Kun Qu,¹ Zhong-Xiao Man,¹ and Zhi-Bin Zhang¹★

¹*School of Physics and Physical Engineering, Qufu Normal University, Qufu, 273165, People's Republic of China*

Accepted XXX. Received YYY; in original form ZZZ

ABSTRACT

Long gamma-ray bursts (LGRBs) are typically thought to result from the collapse of massive stars. Nonetheless, recent observations of gamma-ray bursts (GRBs) 211211A and 230307A, coupled with the low-redshift excess of LGRB event rates relative to star formation rates, present significant challenges to the prevailing model. We reexamine the selection criteria for higher redshift complete GRB samples and identify 280 Swift GRBs with peak flux over $2.6 \text{ ph cm}^{-2} \text{ s}^{-1}$. Assuming all LGRBs with $z \geq 2$ originate from collapsars, we construct the GRB luminosity functions (LFs) in three scenarios: no evolution, luminosity evolution, and density evolution. Our results indicate that a strong redshift evolution in luminosity ($\delta = 1.87^{+0.27}_{-0.31}$) or in density ($\delta = 1.10^{+0.21}_{-0.20}$) is necessary. The luminosity/density evolution model predicts 72.67/57.28 collapsar GRBs at $z < 2$, which can account for 67.29% / 53.04% of the observed LGRBs. This suggests that a substantial portion of LGRBs at $z < 2$ may not be collapsar GRBs, which would challenge the universality of empirical GRB relations and affect their reliability in cosmological applications.

Key words: Gamma-ray bursts – Luminosity function – Star formation

1 INTRODUCTION

Gamma-ray bursts (GRBs) are highly energetic and intense explosions of γ -ray radiation on a short timescale. These events exhibit a diverse array of spectral and temporal characteristics, making them a subject of significant interest in astrophysical research. Since 2004, Swift satellite has detected more than 1,600 GRBs, about 500 out of which have the measured redshifts. Specifically, GRBs are traditionally classified into two categories, that is Long gamma-ray bursts (LGRBs) and short gamma-ray bursts (SGRBs) divided by a duration time of $T_{90} = 2 \text{ s}$. The criterion was verified by KONUS-Wind (Mazets et al. 1981), BATSE (Kouveliotou et al. 1993) and Swift satellites (Zhang & Choi 2008). LGRBs are generally believed to originate from the collapse of massive stars (Woosley 1993; Paczyński 1998), as they are often found in star-forming regions (Totani 1997; Bloom et al. 1998), and a significant fraction of them are found to associate with supernovae (Galama et al. 1998; Kelly et al. 2008; Svensson et al. 2010). Consequently, the event rate of LGRBs is expected to correlate with the star formation rate (SFR) (Elliott et al. 2012; Hao & Yuan 2013; Pescalli et al. 2016). In contrast, SGRBs are believed to originate from mergers of compact binary systems (Berger 2014), as evidenced by their occurrence in regions distant from star-forming areas (Fong et al. 2013) and associations with gravitational wave events (Abbott et al. 2017; Goldstein et al. 2017) or kilonovae (Tanvir et al. 2013; Troja et al. 2019; Fong et al. 2021), suggesting that the event rate of SGRBs may be connected with a delayed SFR (Paul 2018a; Du et al. 2024b).

The origin of LGRBs has recently been challenged. For most astronomical sources, a typical forms of power-law (PL) or broken

power-law (BPL) is usually adopted to describe the luminosity function (LF) (For a more detailed discussion, please refer to Section 5). However, a triple form of the LF is found to exist in LGRBs (Sun et al. 2015; Lan et al. 2021). The triple power-law (TPL) form manifests that the classes of LGRBs may be more complex than before. Recently, Dong et al. (2023) found that the event rate of high-luminosity LGRBs follows the SFR, while the low-luminosity LGRBs exhibits higher event rate than the SFR at the lower redshifts, which indicates that high- and low-luminosity LGRBs should have distinct progenitors. Zhang et al. (2009) found that three LGRBs (050724, 060614 and 061006) exhibit typical characteristics of merger GRBs. In addition, GRB 211211A (Rastinejad et al. 2022) as a LGRB with $T_{90} > 30 \text{ s}$ and $z = 0.076$ was found to associate with a kilonova instead of a traditional supernova. Similarly, GRB 230307A (Levan et al. 2024) with $z = 0.0646$ and $T_{90} \sim 35 \text{ s}$ was identified as abnormal product of a binary neutron star merger. According to the comparison of the event rate of LGRBs with the SFR (Petrosian & Dainotti 2024), it is suggested that more than 60% of LGRBs at $z < 2$ may be non-collapsars.

In this letter, we set the selection criteria to derive an updated complete GRB sample and study the composition of low-redshift LGRBs. In Section 2, we elaborate the sample selection and construct their LF in Section 3. Section 4 presents our results, and the final section provides a concise discussion of our findings.

2 SAMPLES

Since 2004, the Swift satellite has detected more than 1,600 GRBs, among which approximately 500 have measured redshifts. To construct a complete LGRB ($T_{90} > 2 \text{ s}$) sample following the criteria

★ E-mail: z_b_zhang@sina.com (ZHB)

outlined by Jakobsson et al. (2006), Salvaterra et al. (2012) summarized five key selection criteria: (1) The burst must be accurately localized by Swift/XRT, with its coordinates rapidly disseminated; (2) The Galactic extinction along the line of sight to the burst should be low ($A_V < 0.5$); (3) The declination of the GRB must fall within the range $-70^\circ < \delta < 70^\circ$; (4) The angle between the Sun and the field of the burst must exceed 55° ($\theta_{\text{Sun}} > 55^\circ$); and (5) There should be no nearby bright stars that could interfere with observations.

Applying these selection criteria to Swift data up to 2011, Salvaterra et al. (2012) identified 58 LGRBs, of which 52 had measured redshifts, resulting in a redshift completeness of 90%. Later, Pescalli et al. (2016) updated the dataset through July 2014 using the same criteria, identifying 99 LGRBs with 82 having measured redshifts, reducing the redshift completeness to 82%. We applied the aforementioned criteria to Swift LGRBs detected from 2004 to 2023, identifying a total of 160 LGRBs with a redshift completeness reduced to 68%. Figure 1 illustrates the variation in redshift completeness of GRB samples selected according to Salvaterra’s criteria over the years. Interestingly, the redshift completeness shows a declining trend over time, possibly due to a decreasing fraction of GRBs with well-localized follow-up observations.

As shown in Figure 1, the redshift completeness declines significantly over time upon applying the Salvaterra criterion. This observation raises concerns about the suitability of the Salvaterra criteria for current Swift data, prompting us to seek new selection criteria. Similar to the effect of the peak flux threshold on the redshift completeness (Dong et al. 2023), other selection criteria, such as XRT error and Galactic extinction, can also significantly affect the redshift completeness. However, overly stringent criteria can lead to a rapid decline in the sample size. In extreme cases, redshift completeness can approach 100%, but the sample size may reduce to fewer than ten events, which is clearly undesirable. Therefore, when determining the selection criteria, it is crucial to balance redshift completeness and sample size. We define the evaluation metric for the selection criteria as $F = N \times C^3$, where N is the ratio of the number of samples after filtering to the total number of Swift bursts, and C is the redshift completeness after filtering. We maintain the condition of peak flux $P \geq 2.6 \text{ ph cm}^{-2} \text{ s}^{-1}$ and utilize XRT error, Galactic extinction (A_V), GRB declination (δ), and Sun-to-field distance (θ_{Sun}) as free parameters to search for the parameters that maximize the corresponding F-value. The optimal parameters identified are (1) XRT error $< 4.59^\circ$, (2) $A_V < 0.63$, (3) $|\delta| < 75.37^\circ$, and (4) $|\theta_{\text{Sun}}| > 9.87^\circ$. The resulting sample comprises 280 GRBs, among which 167 have measured redshift, exhibiting a redshift completeness of 60%. In comparison to the sample derived from the direct application of the Salvaterra criteria, the redshift completeness decreases by 8%, while the sample size increases by 75%, representing a reasonable trade-off.

Table 2 lists 280 Swift LGRBs that meet our selection criteria, which are categorized into three distinct groups with $z \geq 2$, $z < 2$, and no redshift measurements. Of these, 59 LGRBs are classified into the high-redshift group ($z \geq 2$). It was found that the observed event rate of LGRBs with $z \geq 2$ shows a trend closely matching the SFR (Yu et al. 2015; Tsvetkova et al. 2017; Petrosian & Dainotti 2024), supporting the hypothesis that they are predominantly collapsars. In this work, we constructed the LF for high-redshift LGRBs with $z \geq 2$ and extend to the lower redshift.

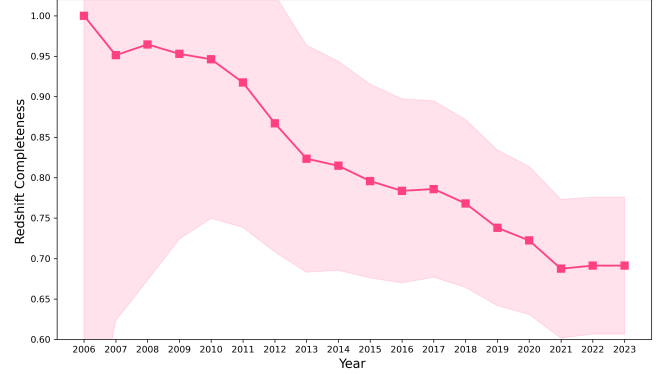


Figure 1. Redshift completeness as a function of observation time for Swift GRB samples selected according to the criteria defined by Salvaterra et al. (2012). The shaded area indicates Poisson errors.

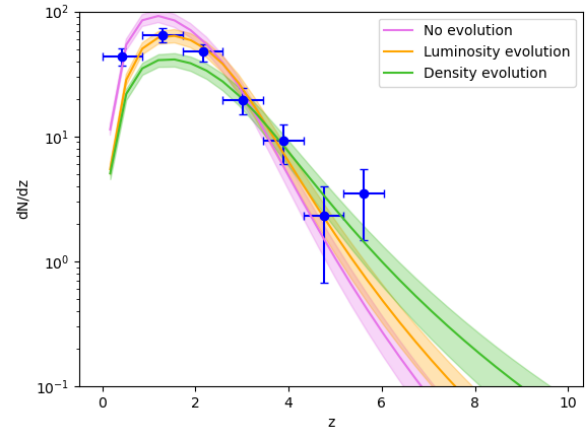


Figure 2. The differential redshift distributions of three theoretical models for collapsar GRBs (color curves). shaded areas indicate the 1σ confidence intervals for each model. The blue data points represent the observed redshift distribution of 167 LGRBs with $P \geq 2.6 \text{ ph cm}^{-2} \text{ s}^{-1}$.

3 ANALYSIS METHOD

We adopted the maximum likelihood method to optimize the free parameters of the model (Marshall et al. 1983; Qu et al. 2019; Narumoto & Totani 2006; Ajello et al. 2009, 2012; Abdo et al. 2010; Zeng et al. 2014, 2016; Lan et al. 2019, 2021, 2022), i.e.,

$$\mathcal{L} = e^{-N_{exp}} \prod_{i=1}^{N_{obs}} \Phi(L_i, z_i, t_i), \quad (1)$$

where N_{exp} and N_{obs} represents the expected and observed numbers of LGRBs, respectively. The term $\Phi(L, z, t)$ denotes the observed rate of GRBs per unit time, within the ranges of z to $z + dz$, L to $L + dL$. The specific form of $\Phi(L, z, t)$ is given by

$$\Phi(L, z, t) = \frac{d^3 N}{dt dz dL} = \frac{d^3 N}{dt dV dL} \times \frac{dV}{dz}, \quad (2)$$

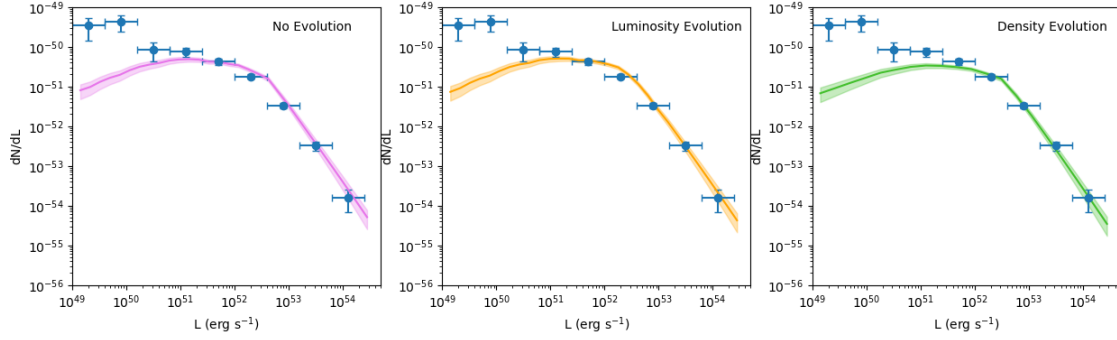


Figure 3. The blue data points show the luminosity distributions of 167 LGRBs with $P \geq 2.6 \text{ ph cm}^{-2} \text{ s}^{-1}$. The solid lines and the shaded regions stand for the luminosity distributions and 1σ scatters of collapsar GRBs as predicted by different models.

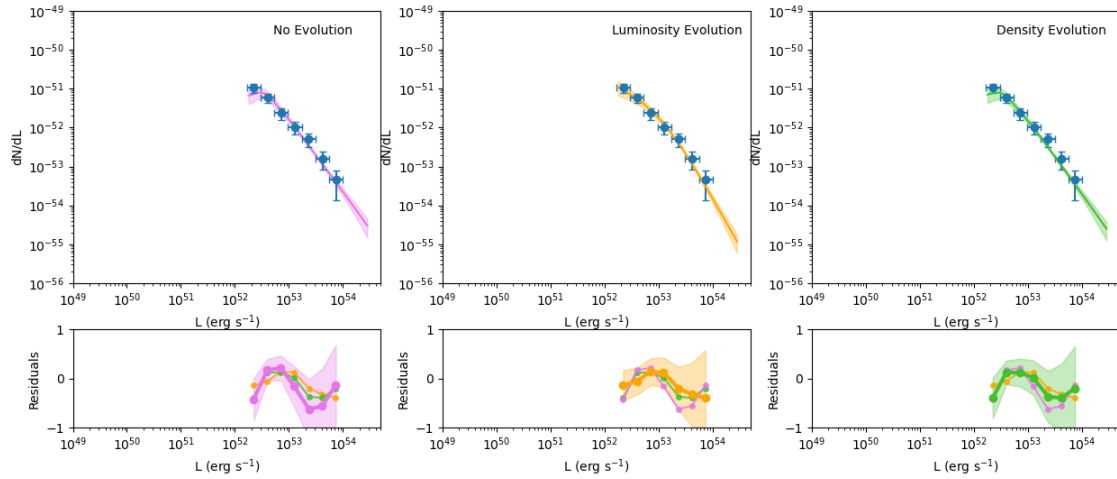


Figure 4. Luminosity distributions of 59 high-redshift ($z \geq 2$) LGRBs with $P \geq 2.6 \text{ ph cm}^{-2} \text{ s}^{-1}$ (solid circles, top row). The top row presents the best-fitting models (solid lines) for three different evolutionary scenarios: no evolution (left), luminosity evolution (middle), and density evolution (right). The shaded regions represent the 1σ confidence intervals. The bottom row displays the residuals corresponding to each model. For each model's residual plot, the residuals for all three models are plotted, with the residuals for the corresponding model shown in bold. The color of the curves in the residual plots corresponds to the color of the respective models in the top row.

Thus

$$\Phi(L, z, t) = \frac{\Delta\Omega}{4\pi} \theta(P) \frac{\psi(z)}{(1+z)} \phi(L, z) \times \frac{dV}{dz}, \quad (3)$$

in which $\Delta\Omega = 1.33 \text{ sr}$ represents the field of view (FOV) of Swift/BAT. $\theta(P)$ indicates the detection efficiency that can be expressed as $\theta(P) \equiv \theta_\gamma(P)\theta_z(P)$, where $\theta_\gamma(P)$ represents the probability of detecting a burst for a given peak flux P . Since our sample is selected with lower limit of $P \geq 2.6 \text{ ph cm}^{-2} \text{ s}^{-1}$, the selection effect is negligible, enabling us to assume $\theta_\gamma(P) = 1$ (Lan et al. 2021). $\theta_z(P)$ corresponds to the probability of measuring the redshift for a given peak flux P . For relatively higher redshift-complete samples (Salvaterra et al. 2012; Pescalli et al. 2016), the term $\theta_z(P)$ was usually approximated to be 1 (Lan et al. 2019), which is reasonable given their redshift completeness exceeding 80%. However, our sample has a redshift completeness of 60%, so we fit with an empirical function to the relationship between $\theta_z(P)$ and P , as $\theta_z(P) = (1 + (1.28 \pm 0.21) \times (0.95 \pm 0.01)^P)^{-1}$. Under the collapsar hypothesis, the GRB event rate, $\psi(z)$, is expected to intrinsically follow the SFR, $\psi_\star(z)$, namely $\psi(z) = \eta\psi_\star(z)$, where η denotes the

efficiency of GRB formation. Following Hopkins & Beacom (2006) and Li (2008), the SFR, $\psi_\star(z)$, can be described by as:

$$\psi_\star(z) = \frac{0.0157 + 0.118z}{1 + (z/3.23)^{4.66}} [M_\odot \text{ yr}^{-1} \text{ Mpc}^{-3}], \quad (4)$$

The function $\phi(L, z)$ represents the normalized GRB LF, which may evolve with redshift depending on the detailed model below. Here, we adopt a generic form of a broken power-law as:

$$\phi(L, z) = \frac{A}{\ln(10)L} \begin{cases} \left(\frac{L}{L_c(z)}\right)^a, & L \leq L_c(z) \\ \left(\frac{L}{L_c(z)}\right)^b, & L > L_c(z) \end{cases}, \quad (5)$$

where A is the normalization constant, a and b are the power-law indices corresponding to luminosities below and above the break luminosity $L_c(z)$, respectively.

The expected number of GRBs can be expressed as

$$N_{\text{exp}} = \frac{\Delta\Omega T}{4\pi} \int_{z_{\text{min}}}^{z_{\text{max}}} \int_{\max[L_{\text{min}}, L_{\text{lim}}(z)]}^{L_{\text{max}}} \theta(P(L, z)) \frac{\psi(z)}{1+z} \times \phi(L, z) dL \frac{dV}{dz} dz, \quad (6)$$

The luminosity threshold in Eq. (6) can be computed by:

$$L_{\text{lim}}(z) = 4\pi D_L^2(z) P_{\text{lim}} \frac{\int_{15 \text{ keV}}^{10^4/(1+z) \text{ keV}} EN(E) dE}{\int_{15 \text{ keV}}^{150 \text{ keV}} N(E) dE}, \quad (7)$$

where P_{lim} represents the peak flux threshold of our sample, that is $P_{\text{lim}} = 2.6 \text{ ph cm}^{-2} \text{ s}^{-1}$. $N(E)$ describes the GRB photon spectrum, that is generally modeled by a Band function (Band et al. 1993; Kaneko et al. 2006), with low (high) energy spectral indices of -1 (-2.3).

To account for (i) the potential biases in the relationship between GRB event rates and the SFR, and (ii) how GRB LF evolves with redshift, we introduce an additional evolutionary factor of $(1+z)^\delta$ into the Eq (6), in which δ is a free parameter. We investigate three distinct models: (1) the GRB event rate follows the SFR directly, i.e., $\psi(z) = \eta\psi_\star(z)$, with a non-evolving LF, i.e., $L_{ci}(z) = L_{ci,0}$ (constant); (2) the GRB event rate is proportional to the SFR, but the LF's break luminosity evolves with redshift, as $L_{ci}(z) = L_{ci,0}(1+z)^\delta$; and (3) the GRB event rate includes an additional evolutionary factor, say $\psi(z) = \eta\psi_\star(z)(1+z)^\delta$, while the LF is assumed to be independent of redshift.

Once the optimal parameters for each model are determined, we substitute them into Eq. (6), and set the redshift integration limits from $z_{\text{min}} = 0$ to $z_{\text{max}} = 2$. This allows us to compute the expected number of collapsar GRBs between redshifts 0 and 2 of any one of the above three models.

4 RESULTS

We applied the MCMC method to optimize the model's free parameters (Goodman & Weare 2010; Foreman-Mackey et al. 2013), specifically the GRB LF, the evolution parameter, and the formation efficiency η . Afterward, we computed the corresponding maximum likelihood estimation, Akaike Information Criterion (AIC), and Bayesian Information Criterion (BIC). The results are summarized in Table 1. Figures 2 and 3 illustrate the redshift and luminosity distributions of 167 GRBs with measured redshift and $P \geq 2.6 \text{ ph cm}^{-2} \text{ s}^{-1}$ in our sample. The solid lines represent the extrapolated redshift and luminosity distributions by extending the LF, which was fitted to the high-redshift sample but down to $z = 0$. In other words, in Figure 2, the data points represent the redshift distribution of the LGRBs, while the solid lines show the redshift distributions of the collapsar GRBs derived from three different model. Similarly, in Figure 3, the data points represent the luminosity distribution of the LGRBs, and the solid lines correspond to the luminosity distribution of the collapsar GRBs as derived in this study.

In Figure 2, the redshift distribution of collapsar GRBs obtained from the no-evolution model (the pink solid line) is noticeably higher at low redshifts than the redshift distribution of LGRBs (the blue data points). It is worth noting that similar results have been observed in previous studies of the LGRB LFs (Salvaterra et al. 2012; Lan et al. 2019, 2021), where the no-evolution model also shows a significantly higher redshift distribution at low redshifts compared to the observed distribution. This discrepancy is attributed to the fact that an evolution

term is essential for the LF of LGRBs, and the no-evolution model fails to adequately fit the data.

Within the luminosity evolution model framework, the GRB event rate exhibits more close to the SFR. However, the characteristic break luminosity of the GRB LF evolves with the redshift, namely $L_c(z) = L_{c,0}(1+z)^\delta$. Utilizing a BPL LF, our analysis demonstrates notable luminosity evolution, yielding a value of $\delta = 1.87^{+0.27}_{-0.31}$. This result is consistent with previous parametric studies (e.g., Salvaterra et al., 2012, Lan et al., 2019). Additionally, this value is roughly consistent with estimates obtained using non-parametric methods (e.g., Lloyd-Ronning et al., 2002, Petrosian et al., 2015, Yu et al., 2015, Pescalli et al., 2016, Dong et al. 2022, 2023). Based on the optimal parameters of the luminosity evolution model, we calculate the expected number of collapsar GRBs within the range of $0 < z < 2$. By adjusting the limits of integration in Eq. (6) to this range, the luminosity evolution model predicts that the number of collapsar GRBs with $z < 2$ and $P \geq 2.6 \text{ ph cm}^{-2} \text{ s}^{-1}$ is 72.67, representing 67.29% of the observed LGRBs. This indicates that approximately 32.71% of low-redshift LGRBs are likely not associated with collapsars.

The density evolution model assumes that the break luminosity in the GRB LF remains constant, while the GRB event rate behaves a redshift-dependent feature of $\psi(z) = \eta\psi_\star(z)(1+z)^\delta$. Using the BPL LF again, one can constrain the density evolution to be $\delta = 1.10^{+0.21}_{-0.20}$. We apply Eq. (6) to estimate the expected number of collapsar GRBs within the redshift range of $0 < z < 2$. As a result, the density evolution model predicts that the number of collapsar GRBs with $z < 2$ and $P \geq 2.6 \text{ ph cm}^{-2} \text{ s}^{-1}$ is 57.28, corresponding to 53.04% of the observed LGRBs. This indicates that approximately 47% of low-redshift LGRBs may non-collapsars.

It can be seen from Figure 2 that at low redshifts, the redshift distribution of the collapsar LF obtained from the luminosity evolution (yellow solid line) and density evolution (green solid line) is significantly lower than the redshift distribution of observed LGRBs (the blue data points). Our findings are in good agreement with the results of Petrosian & Dainotti (2024), who found that approximately 60% of LGRBs with $z < 2$ are not collapsar events.

From the perspective of luminosity distribution (Fig. 3), the luminosity distribution of collapsar GRBs (solid line) is significantly lower than that of LGRBs (the blue data points) in the low-luminosity part. This is consistent with the findings of Dong et al. (2023), which show that the event rate of high-luminosity LGRBs follows the SFR well, while the event rate of low-luminosity LGRBs deviates significantly from the SFR, providing mutual confirmation.

To demonstrate that our model fits the sample well, we present in Figure 4 the luminosity distributions (solid circles) of 59 high-redshift ($z \geq 2$) LGRBs with $P \geq 2.6 \text{ ph cm}^{-2} \text{ s}^{-1}$, which is the high-redshift collapsar sample used for our fit, as well as the luminosity distributions for $z > 2$ from the three models. In the second row of Figure 4, we plot the residuals for each model. The residuals are defined as $Residuals = \frac{dN/dL_{\text{theory}} - dN/dL_{\text{obs}}}{dN/dL_{\text{theory}}}$. For each model's residual plot, the residuals for all three models are plotted, with the residuals for the corresponding model shown in bold. The color of the curves in the residual plots corresponds to the color of the respective models in the top row. From the perspective of luminosity distribution, all three models provide a good fit to the sample. From the residual plot, the no-evolution model slightly underperforms compared to the other two models.

It should be emphasized that we are not directly fitting the luminosity and redshift distributions, but instead obtaining the best-fit parameters via the maximum likelihood method using Equation (1).

We also use AIC and BIC to evaluate the relative performance of the models.

After obtaining the AIC for each model, we can use the Akaike weight $\exp(-AIC_i/2)$ to judge the confidence level of one model relative to another. The relative probability of the i^{th} model being preferred is defined specifically as :

$$P(M_i) = \frac{e^{-AIC_i/2}}{e^{-AIC_1/2} + e^{-AIC_2/2}}, \quad (8)$$

Based on the AIC, the probability that the no-evolution model is correct compared to the luminosity evolution model is only 0.001. Furthermore, the difference in BIC values between the no-evolution model and the luminosity evolution model is 8.12, which is sufficient to rule out the no-evolution model.

5 CONCLUSION AND DISCUSSION

We re-assessed the selection criteria for high redshift-completeness GRB samples and applied the updated criteria to identify a sample of 280 GRBs with peak flux $P \geq 2.6 \text{ ph cm}^{-2} \text{ s}^{-1}$, which is 2.8 times larger than the BAT6ext sample (Pescalli et al. 2016). Using GRBs with $z \geq 2$, we constructed the LF and evaluated three evolutionary scenarios including no evolution, luminosity evolution, and density evolution. Our analysis shows that the no evolution scenario can be ruled out, while both the luminosity evolution and the density evolution models fit the observed data well. The luminosity evolution model predicts that the number of collapsar GRBs with $z < 2$ and $P \geq 2.6 \text{ ph cm}^{-2} \text{ s}^{-1}$ is 72.67, accounting for 67.29% of the observed LGRBs. Similarly, the density evolution model predicts that the number of collapsar GRBs under the same conditions is 57.28, representing 53.04% of the observed LGRBs. Our results confirm that the majority of low-redshift ($z < 2$) LGRBs are produced from the collapsar rather than the non-collapsar progenitors. Our study suggests that LGRBs originating from sources other than massive star collapses may not be rare occurrences. In fact, for redshifts below 2, the fraction could be as high as 33% under the luminosity evolution model, and up to 47% under the density evolution model.

As of 2009, Zhang et al. (2009) identified three LGRBs (050724, 060614 and 061006) as the Type I burst, of which their progenitors were likely mergers of two compact stars. More recently, further evidence has emerged for additional LGRBs with strong indications of compact star mergers as progenitors, such as GRB 211211A (Rastinejad et al. 2022) and GRB 230307A (Levan et al. 2024), as well as GRB 170228A, which exhibits similar characteristics (Wang et al. 2024).

Regarding the luminosity distributions, how to choose the function is still controversial. For example, Sun et al. (2015) identified that the LF of LGRBs is best described by a TPL. Similarly, Lan et al. (2021) using a larger Swift sample, reported consistent findings. It is noteworthy that a TPL is an uncommon form for LFs. In contrast, Sun et al. (2015) found that the LFs of other extragalactic high-energy transients, such as SGRBs, supernova shock breakouts (SBOs), and tidal disruption events (TDEs), typically follow a single power law rather than a TPL. A plausible explanation for the TPL in the LGRB LF is the inclusion of a subset of non-collapsar bursts. These non-collapsar bursts may exhibit a BPL LF with a lower luminosity, while collapsar bursts have their own BPL LF with higher luminosity. The combination of these two components could cause the LGRB LF to appear as a TPL. Dong et al. (2023) classified LGRBs into high- and low-luminosity groups and calculated their event rates separately. Their analysis revealed that the event rate of high-luminosity GRBs

closely follows the SFR, whereas the event rate of low-luminosity GRBs deviates significantly, further supporting this argument.

The nature of non-collapsar LGRBs at low redshift still remains an open question. One plausible hypothesis suggests that non-collapsar LGRBs may originate from compact binary mergers, such as black hole–black hole mergers (Bavera et al. 2022) or white dwarf–black hole mergers (Lloyd-Ronning et al. 2024). However, several non-compact star merger scenarios have also been proposed, such as helium mergers (or similar type) systems (Lloyd-Ronning et al. 2019), and the collapse of massive stars in interacting binary systems (Lloyd-Ronning 2022). If the progenitors of these LGRBs are stars, their event rate should correlate with the SFR. In contrast, if they arise from compact binary mergers, their event rate would be associated with the delayed SFR (Paul 2018b; Du et al. 2024a). Constructing LFs based on both SFR and delayed SFR, and fitting the excess in the dN/dZ and dN/dL distributions seen in Figures 2 and 3 compared to the predictions for collapsar GRBs, may help identify the origins of these non-collapsar GRBs.

ACKNOWLEDGEMENTS

This work was supported in part by National Natural Science Foundation of China (grant No. U2031118) .

DATA AVAILABILITY

All data used in this paper are public.

REFERENCES

- Abbott B. P., et al., 2017, *Phys. Rev. Lett.*, **119**, 161101
 Abdo A. A., et al., 2010, *ApJ*, **720**, 435
 Ajello M., et al., 2009, *ApJ*, **699**, 603
 Ajello M., et al., 2012, *ApJ*, **751**, 108
 Amati L., Guidorzi C., Frontera F., Della Valle M., Finelli F., Landi R., Montanari E., 2008, *MNRAS*, **391**, 577
 Amati L., Frontera F., Guidorzi C., 2009, *A&A*, **508**, 173
 Amati L., D’Agostino R., Luongo O., Muccino M., Tantalò M., 2019, *MNRAS*, **486**, L46
 Band D., et al., 1993, *ApJ*, **413**, 281
 Bavera S. S., et al., 2022, *A&A*, **657**, L8
 Berger E., 2014, *ARA&A*, **52**, 43
 Bissaldi E., Meegan C., 2017, GRB Coordinates Network, **21297**, 1
 Bloom J. S., Djorgovski S. G., Kulkarni S. R., Frail D. A., 1998, *ApJ*, **507**, L25
 Butler N. R., Kocevski D., Bloom J. S., Curtis J. L., 2007, *ApJ*, **671**, 656
 Dong X. F., Li X. J., Zhang Z. B., Zhang X. L., 2022, *MNRAS*, **513**, 1078
 Dong X. F., Zhang Z. B., Li Q. M., Huang Y. F., Bian K., 2023, *ApJ*, **958**, 37
 Du X., Zhang Z. B., Li G. A., et al., 2024a, Event rates of short gamma-ray bursts originated from compact binary mergers in the era of multiple missions, To be submitted to *ApJL*
 Du X. Y., Zhen H. Y., Liu J. X., Zhang Z. B., Dong X. F., Ge Y., Yan J. M., 2024b, *ApJ*, **960**, 77
 Elliott J., Greiner J., Khochfar S., Schady P., Johnson J. L., Rau A., 2012, *A&A*, **539**, A113
 Fong W., et al., 2013, *ApJ*, **769**, 56
 Fong W., et al., 2021, *ApJ*, **906**, 127
 Foreman-Mackey D., Hogg D. W., Lang D., Goodman J., 2013, *PASP*, **125**, 306
 Frederiks D., et al., 2016, GRB Coordinates Network, **20082**, 1
 Frederiks D., et al., 2017, GRB Coordinates Network, **20604**, 1
 Frederiks D., et al., 2018, GRB Coordinates Network, **22546**, 1
 Galama T. J., et al., 1998, *Nature*, **395**, 670

Table 1. Parameters of the best fit with different models.

Model	Evolution parameter	η ($10^{-8} M_{\odot}^{-1}$)	a	b	$\log L_c$ (erg s^{-1})	$\ln \mathcal{L}$	AIC	BIC
No evolution	...	$8.78^{+1.17}_{-1.19}$	$-0.08^{+0.02}_{-0.02}$	$-1.07^{+0.18}_{-0.17}$	$52.57^{+0.13}_{-0.14}$	-82.85	173.70	182.01
Luminosity evolution	$\delta = 1.87^{+0.27}_{-0.31}$	$6.69^{+0.95}_{-0.93}$	$-0.29^{+0.05}_{-0.05}$	$-1.59^{+0.19}_{-0.18}$	$52.20^{+0.11}_{-0.12}$	-76.75	161.5	173.89
Density evolution	$\delta = 1.10^{+0.21}_{-0.20}$	$4.23^{+0.83}_{-0.85}$	$-0.21^{+0.03}_{-0.03}$	$-1.11^{+0.21}_{-0.19}$	$52.54^{+0.10}_{-0.11}$	-76.89	161.78	174.17

Note. The parameter values were determined as the medians of the best-fitting parameters from the Monte Carlo sample. The errors represent the 68% containment regions around the median values.

Table 2. List of 280 Swift GRBs that meet our selection criteria.

GRBs with $z \geq 2$											
GRB	Ref	GRB	Ref	GRB	Ref	GRB	Ref	GRB	Ref	GRB	Ref
050603	3	070714A	3	090201	1, 3	120811C	15	150206A	1, 4	190719C	1, 11
050922C	1, 3	080413A	2, 3	090715B	16	121209A	1, 3	150403A	1, 4	191004B	2, 12
051008	1, 4	080603B	14	090812	16	130427B	1, 3	150424A	1, 2	210112A	1, 2
051109A	13	080607	14	100704A	2, 3	130505A	1, 4	151021A	1, 5	220101A	1, 2
060206	1, 4	080721	14	100728B	1, 3	130514A	1, 3	161014A	1, 4	220521A	1, 2
060210	15	080804	15	110205A	1, 3	130606A	1, 3	161017A	1, 6	230818A	1, 2
060927	13	081121	14	110709B	1, 3	140206A	16, 17	170202A	1, 7	231210B	1, 2
061222A	2, 3	081203A	2, 3	110731A	1, 3	140419A	1, 3	170705A	1, 8	221226B	1, 2
070328	1, 4	081221	15	111008A	1, 3	140629A	1, 3	180325A	1, 9	210411C	1, 2
070521	15	081222	14	120802A	1, 3	140703A	1, 3	181020A	1, 10		
GRBs with $z < 2$											
050219A	050318	050416A	050525A	050802	051111	060306	060418	060505	060614	060814	060908
060912A	061007	061021	061121	061126	070306	070714B	071112C	071117	080319B	080319C	080411
080413B	080430	080602	080605	080916A	081007	090102	090424	090709A	090926B	091018	091020
091127	091208B	100615A	100621A	100728A	100816A	110422A	111228A	120119A	120326A	120729A	120907A
130420A	130427A	130701A	130831A	130907A	130925A	131030A	131105A	140213A	140506A	140512A	141220A
141221A	150301B	150314A	150323A	151027A	160131A	160410A	160425A	160703A	160804A	161001A	161117A
161129A	161219B	170604A	170903A	180205A	180314A	180620B	180720B	181110A	190106A	190114C	190324A
190829A	191019A	191221B	200528A	200829A	201024A	201104B	201216C	201221D	210104A	210207B	210210A
210217A	210410A	210610B	210619B	210822A	211211A	211227A	220427A	230325A	231111A	231117A	231118A
GRBs without redshift											
050124	050128	050219B	050326	060105	080218B	080229A	080613B	090929B	091221	100522A	100619A
101017A	110102A	110402A	110420A	110709A	110915A	120102A	120116A	120311A	120703A	121123A	121125A
130502A	130527A	130609B	130727A	130803A	130812A	131128A	140102A	140215A	140529A	140619A	140628A
140716A	140817A	141005A	141017A	141212B	150222A	150428A	150430A	150607A	150616A	150710B	150711A
151114A	160119A	160216A	160325A	160424A	160607A	161117B	170126A	170208A	170208B	170317A	170626A
170803A	170822A	170906A	170906C	171027A	171120A	180111A	180331B	180404B	180418A	180620A	180626A
180706A	180809B	180925A	181126A	190103B	190202A	190511A	190604B	190613B	190824A	191004A	191031C
191122A	200122A	200125A	200131A	200215A	200303A	200306A	200416A	200716C	200901A	200922A	201013A
201209A	210226A	210305A	210306A	210514A	210730A	220118A	220408A	220714B	220826A	221016A	221027B
221201A	230228A	230510A	230606A	231205B							

Note: 280 Swift GRB used in this study. The spectra and redshift references are from the following sources: (1) <https://www.mpe.mpg.de/~jcg/grbgen.html>; (2) <https://swift.gsfc.nasa.gov/archive/grbtable/>; (3) Wang et al. (2020); (4) Butler et al. (2007); (5) Golenetskii et al. (2015); (6) Frederiks et al. (2016); (7) Frederiks et al. (2017); (8) Bissaldi & Meegan (2017); (9) Frederiks et al. (2018); (10) Tsvetkova et al. (2018); (11) Poolakkil et al. (2019); (12) Svinin et al. (2019); (13) Amati et al. (2008); (14) Amati et al. (2009); (15) Amati et al. (2019); (16) Wang et al. (2016); (17) von Kienlin et al. (2020);

Goldstein A., et al., 2017, *ApJ*, **848**, L14

Golenetskii S., et al., 2015, GRB Coordinates Network, **18433**, 1

Goodman J., Weare J., 2010, *Communications in Applied Mathematics and Computational Science*, **5**, 65

Hao J.-M., Yuan Y.-F., 2013, *ApJ*, **772**, 42

Hopkins A. M., Beacom J. F., 2006, *ApJ*, **651**, 142

Jakobsson P., et al., 2006, *A&A*, **447**, 897

Kaneko Y., Preece R. D., Briggs M. S., Paciasas W. S., Meegan C. A., Band D. L., 2006, *ApJS*, **166**, 298

Kelly P. L., Kirshner R. P., Pahre M., 2008, *ApJ*, **687**, 1201

Kouveliotou C., Meegan C. A., Fishman G. J., Bhat N. P., Briggs M. S., Koshut T. M., Paciasas W. S., Pendleton G. N., 1993, *ApJ*, **413**, L101

Lan G.-X., Zeng H.-D., Wei J.-J., Wu X.-F., 2019, *MNRAS*, **488**, 4607

Lan G.-X., Wei J.-J., Zeng H.-D., Li Y., Wu X.-F., 2021, *MNRAS*, **508**, 52

Lan G.-X., Wei J.-J., Li Y., Zeng H.-D., Wu X.-F., 2022, *ApJ*, **938**, 129

Levan A. J., et al., 2024, *Nature*, **626**, 737

Li L.-X., 2008, *MNRAS*, **388**, 1487

Lloyd-Ronning N., 2022, *ApJ*, **928**, 104

Lloyd-Ronning N. M., Fryer C. L., Ramirez-Ruiz E., 2002, *ApJ*, **574**, 554

Lloyd-Ronning N. M., Gompertz B., Pe'er A., Dainotti M., Fruchter A., 2019, *ApJ*, **871**, 118

Lloyd-Ronning N. M., Johnson J. L., Upton Sanderbeck P. R., Silva M., Cheng R. M., 2024, *arXiv e-prints*, p. [arXiv:2408.12654](https://arxiv.org/abs/2408.12654)

Marshall H. L., Tananbaum H., Avni Y., Zamorani G., 1983, *ApJ*, **269**, 35

Mazets E. P., et al., 1981, *Ap&SS*, **80**, 3

Narumoto T., Totani T., 2006, *ApJ*, **643**, 81

- Paczynski B., 1998, *ApJ*, 494, L45
- Paul D., 2018a, *MNRAS*, 473, 3385
- Paul D., 2018b, *MNRAS*, 477, 4275
- Pescalli A., et al., 2016, *A&A*, 587, A40
- Petrosian V., Dainotti M. G., 2024, *ApJ*, 963, L12
- Petrosian V., Kitanidis E., Kocevski D., 2015, *ApJ*, 806, 44
- Poolakkil S., Meegan C., Fermi GBM Team 2019, GRB Coordinates Network, 25130, 1
- Qu Y., Zeng H., Yan D., 2019, *MNRAS*, 490, 758
- Rastinejad J. C., et al., 2022, *Nature*, 612, 223
- Salvatterra R., et al., 2012, *ApJ*, 749, 68
- Sun H., Zhang B., Li Z., 2015, *ApJ*, 812, 33
- Svensson K. M., Levan A. J., Tanvir N. R., Fruchter A. S., Strolger L. G., 2010, *MNRAS*, 405, 57
- Svinkin D., et al., 2019, GRB Coordinates Network, 25974, 1
- Tanvir N. R., Levan A. J., Fruchter A. S., Hjorth J., Hounsell R. A., Wiersema K., Tunnicliffe R. L., 2013, *Nature*, 500, 547
- Totani T., 1997, *ApJ*, 486, L71
- Troja E., et al., 2019, *MNRAS*, 489, 2104
- Tsvetkova A., et al., 2017, *ApJ*, 850, 161
- Tsvetkova A., et al., 2018, GRB Coordinates Network, 23363, 1
- Wang J. S., Wang F. Y., Cheng K. S., Dai Z. G., 2016, *A&A*, 585, A68
- Wang F., Zou Y.-C., Liu F., Liao B., Liu Y., Chai Y., Xia L., 2020, *ApJ*, 893, 77
- Wang C.-W., et al., 2024, *arXiv e-prints*, p. arXiv:2407.02376
- Woosley S. E., 1993, *ApJ*, 405, 273
- Yu H., Wang F. Y., Dai Z. G., Cheng K. S., 2015, *ApJS*, 218, 13
- Zeng H., Yan D., Zhang L., 2014, *MNRAS*, 441, 1760
- Zeng H., Melia F., Zhang L., 2016, *MNRAS*, 462, 3094
- Zhang Z. B., Choi C. S., 2008, *A&A*, 484, 293
- Zhang B., et al., 2009, *ApJ*, 703, 1696
- von Kienlin A., et al., 2020, *ApJ*, 893, 46

This paper has been typeset from a $\text{\TeX}/\text{\LaTeX}$ file prepared by the author.